CRYSTAL GROWTH & DESIGN

pubs.acs.org/crystal

Article

DNA Nanoflowers Assemble via Template-Induced Crystallization during mRNA Synthesis

Soroush Ahmadi, Nathan M. Stover, Krystian Ganko, Frances B. Kayser, Richard D. Braatz, and Allan S. Myerson*

Cite This: *Cryst. Growth Des.* 2026, 26, 2108−2117

Read Online

ACCESS | Metrics & More | Article Recommendations | Supporting Information

ABSTRACT: mRNA-based vaccines and therapeutics are synthesized using the *in vitro* transcription (IVT) reaction. However, the byproduct pyrophosphate (PPi) forms insoluble magnesium pyrophosphate (Mg_2PPi) during IVT, which coprecipitates with DNA, the transcription blueprint, interrupting the reaction and reducing RNA yield. The severity of this crystallization problem has prompted the routine inclusion of inorganic pyrophosphatase (PPase) in industrial processes to hydrolyze pyrophosphate into phosphate ions and prevent crystallization. To date, the mechanism by which Mg_2PPi crystals interact with DNA has remained unclear. In this work, we demonstrate that DNA promotes Mg_2PPi crystallization through a template-directed mechanism, reducing the nucleation induction time by a factor of 2. The resulting crystals form compact spherulites with a rosette habit, distinct from the morphologies observed in DNA-free systems. We propose that DNA preferentially templates the nucleation of $Mg_2PPi{\cdot}3.5H_2O$ crystals by interacting with the {100} crystal face. These findings reveal how DNA influences Mg_2PPi crystallization and offer mechanistic insights relevant to optimizing RNA manufacturing systems.

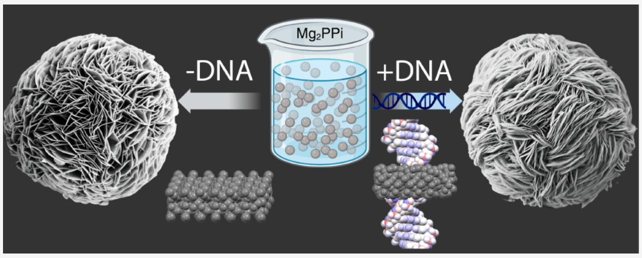

1. INTRODUCTION

Nucleic acid amplification reactions are widely used to synthesize RNA and DNA molecules. During these reactions, yarn-like nanoparticles composed of hybrid organic−inorganic materials can form. These composite structures may influence reaction dynamics and yield, and have also been explored for applications in drug delivery, bioseparation, and bioimaging.[1−4] Early studies hypothesized these particles to be single DNA strands that self-assemble into spherical shapes and were investigated as drug delivery vehicles for Cas9 protein[5] and doxorubicin.[6] However, it is now understood that these nanoparticles are, in fact, composite nucleic acid/magnesium pyrophosphate (Mg_2PPi) sponge-like microstructures. These hybrid nucleic acid-inorganic materials are referred to as DNA nanoflowers (DNFs)[7−11] and RNA microsponges (MS).[12−14]

In the context of the *in vitro* transcription (IVT) reaction, these DNFs can be disruptive. As shown in Figure 1, IVT involves a DNA template that serves as a blueprint for RNA synthesis, where RNA nucleotide triphosphates (NTPs) are provided as monomers, and RNA polymerase (typically T7 or SP6) catalyzes their addition to the growing RNA strand. During this process, two phosphate groups (pyrophosphate, or PPi) are cleaved off each NTP, which can result in the crystallization of Mg_2PPi crystals. It has been observed that the IVT reaction stops when this crystallization occurs.[15] It is hypothesized that this reduction in reaction rate is owed to the sequestration of DNA into DNA nanoflowers.[16] This issue is so pronounced that inorganic pyrophosphatase (PPase)[17] is often included in the reaction mixture to hydrolyze pyrophosphate into phosphate ions, thereby mitigating crystallization and maintaining transcriptional activity. Although PPase has proven effective, the formation of magnesium phosphate (MgPi) with low aqueous solubility has been hypothesized and was recently observed and characterized in fed-batch IVT systems.[18] The crystallization mechanism of Mg_2PPi leading to DNF formation remains unclear and warrants further investigation. Given that IVT is the primary industrial method for producing mRNA vaccines and therapies,[19−21] a better mechanistic understanding of this crystallization process can inform strategies for RNA manufacturing.

The mechanism of interaction between DNA and magnesium pyrophosphate has so far remained largely speculative. Two possible pathways are possible: (1) physical adsorption, in which DNA becomes incorporated into Mg_2PPi crystals after nucleation and during the growth, and (2) template-directed nucleation, in which DNA actively promotes crystal nucleation. Previous studies have primarily relied on morphological

Received: December 4, 2025
Revised: January 30, 2026
Accepted: February 2, 2026
Published: February 12, 2026

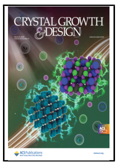

https://doi.org/10.1021/acs.cgd.5c01710
Cryst. Growth Des. 2026, 26, 2108−2117

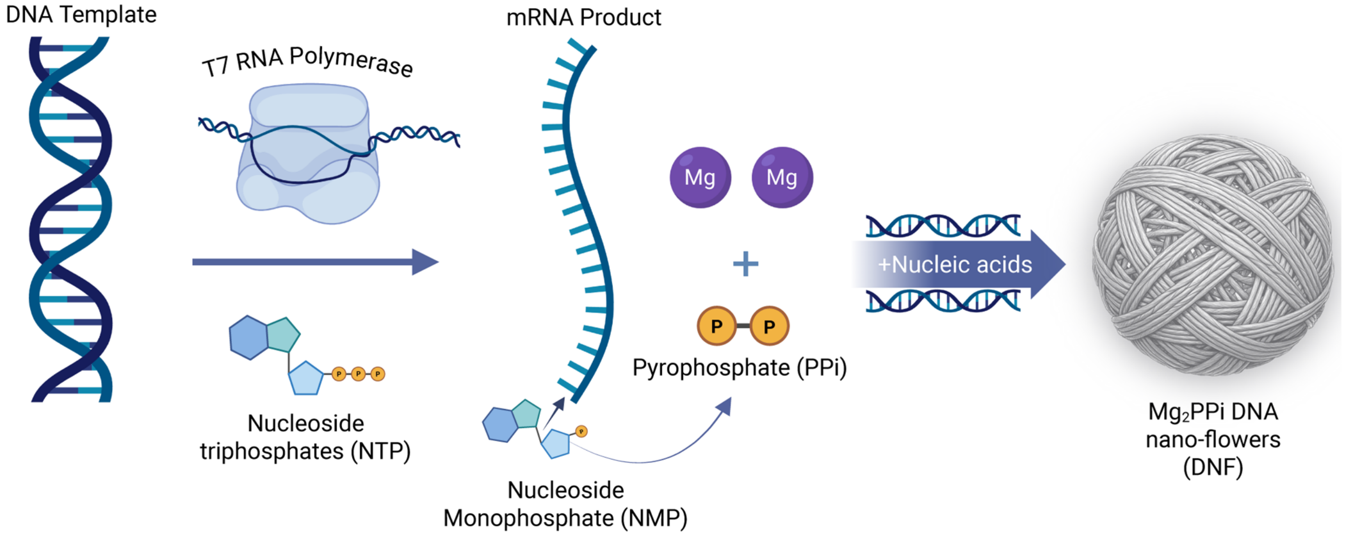

Figure 1. Process of Mg_2PPi crystallization during the IVT reaction. RNA polymerase incorporates NTP monomers into RNA based on the sequence of a DNA template. The pyrophosphate (PPi) byproduct of this reaction can precipitate in the form of Mg_2PPi solid. In the presence of DNA, Mg_2PPi can form as a composite nanoflower.

Table 1. Summary of Crystallization Experiments, Including Reactant Concentrations, Additives, and Corresponding Figures

Experiment	Mg (mM)	PPi (mM)	Spr (mM)	DTT (mM)	ATP (mM)	DNA	Figures
Minimal setup	4.0	0.1−1.0	–	–	–	–	3a, S2, S6
Scaled-up PXRD $6H_2O$	4.0	0.4	–	–	–	–	3b,c, S7
Scaled-up PXRD $3.5H_2O$	4.0	0.7	–	–	–	–	3b,c
Phase diagram	4.0−128.0	0.2−100.0	2	5	4.0, 20.0	–	4b,c
IVT-only	8.0	0.1−1.0	2	5	3.2	–	5, S4a, S5
IVT + DNA	8.0	0.1−1.0	2	5	3.2	+	5, 6, S4b, S5
Minimal + DNA	4.0	0.4	–	–	–	+	6a,b, S6

observations from electron microscopy, proposing that DNA mediates the aggregation process of Mg_2PPi nanoflakes. It has been hypothesized that DNA inhibits Mg_2PPi crystallization by slowing nucleation and growth and that DNA incorporation may alter the lattice structure of the solid precipitate.[9] However, such evidence remains qualitative and inconclusive, leaving the underlying mechanism unresolved.

In this work, we investigate the interactions of DNA and magnesium pyrophosphate precipitates during DNA nanoflower formation and develop an alternate mechanistic understanding of this process. First, we evaluate the effect of solution conditions on Mg_2PPi crystallization and structure, aided by a solution thermodynamic model. Next, we assess the impact of DNA on $Mg_2PPi{\cdot}3.5H_2O$ crystallization using high-throughput kinetic studies. These kinetic measurements are combined with a structural analysis of $Mg_2PPi{\cdot}3.5H_2O$ crystals using X-ray and electron diffraction to fully characterize the formation of composite nanoflowers and their underlying mechanism.

2. EXPERIMENTAL SECTION

2.1. Materials

Magnesium chloride (1 M solution, Biotechnology grade, Avantor), sodium pyrophosphate (200 mM buffer solution, Thermo Scientific), and Tris (1 M, pH 8.0, RNase-free, Thermo Fisher Scientific) were used as purchased. Spermidine ≥99% (GC) (Sigma-Aldrich) was used as supplied and stored at 4 °C until required for experiments. Dithiothreitol (DTT, No-Weigh format, Thermo Scientific) was stored as a solid at 4 °C and freshly dissolved in 40 mM Tris buffer before use. Aliquots of linearized DNA template for saRNA, provided by Arranta, and ATP solution (100 mM), purchased from Thermo Scientific, were stored at −20 °C and thawed as required.

2.2. Studying the Effects of IVT Components on Crystallization

To assess how different components of the IVT reaction mixture influence crystallization under controlled nucleation conditions, experiments were designed in three different stages, progressing from simplified systems to a chemically complete IVT-like mixture. In the most complete stage, the system includes all standard IVT components except RNA polymerase, with concentrations chosen to match typical literature and industrial IVT setups. This design avoids continuous changes in supersaturation due to ongoing PPi release and enables quantitative analysis of Mg_2PPi nucleation kinetics, while keeping the chemical environment of a transcription reaction as close as possible to that of a full IVT system. First, a minimal crystallization setup was prepared with $MgCl_2$ and Na_4PPi in 40 mM Tris buffer at pH 8.0. This served as a reference system to assess crystallization in the absence of additives. To assess the effect of PPi concentration on crystallization, the Mg concentration was fixed at 4 mM, and varying PPi concentrations with a step size of 0.1 mM (ranging from 0.1 to 1 mM) were placed in a row of a well plate. The microplate was sealed and imaged using a Zeiss Axio Observer 7 microscope for 72 h of time-lapse recording, after which the experiments were continued for 2 weeks to allow complete equilibration. The final frame images are reported. In the second set of experiments, small molecule additives commonly used in IVT reactions, including spermidine (Spr), dithiothreitol (DTT), and adenosine triphosphate (ATP), were introduced to investigate their influence on nucleation and growth behavior. The third set of experiments included the full IVT reaction mixture with linearized DNA template, but without the RNA polymerase enzyme to prevent transcription from initiating. This allowed the isolation of DNA effects on crystallization. By comparing crystallization across these different conditions, the specific contributions of small molecules and macromolecules to nucleation kinetics, growth rates, and crystal morphology are distinguished. Table 1 summarizes the experimental conditions.

2.3. Speciation Modeling

To predict the thermodynamic supersaturation of Mg_2PPi in the IVT solution, we modeled the ionic speciation of magnesium, pyrophosphate, sodium, NTP, and spermidine ions based on an approach outlined in previous work.[16] This approach combines equations governing speciation equilibria with mass balances for each species in the reaction mixture. The equilibrium constants used in this model are shown in Table S1. The full code for this model and the visualizations presented in this work is contained at github.com/nathanmstover/IVTsolutionthermo.

2.4. High-Throughput Nucleation and Growth Rate Determination

Crystal nucleation[22] is difficult to observe experimentally due to the small size of initial clusters, which move freely in solution and are hard to track. Once the nuclei grow to a detectable size and settle at the bottom of the well, time-lapse microscopy becomes the most reliable tool for detecting them and determining induction time. The nucleation rate can then be calculated by fitting the cumulative distribution of induction times to a Poisson distribution. Nucleation is a stochastic process in which the probability of a single molecular collision leading to crystal formation is extremely low, while the number of potential collisions is extremely large. Under these conditions, the Poisson distribution naturally arises as the limit of the binomial distribution when the probability of success is very small and the number of trials is very large, making it suitable for modeling the distribution of induction times. Here, nucleation and growth rates were determined using a Zeiss Axio Observer 7 inverted microscope. Cellvis 96-well glass bottom plates with high-performance cover glass served as microbatch crystallizers. After loading 200 μL microbatches of IVT-only and IVT +DNA conditions (40 to 80 replicates per supersaturation), the wells were sealed to prevent evaporation. The sealed plates were placed between a PeCon GmbH Heating Insert M96 2000 EC and an Incubator P S compact, both heated to maintain a constant temperature 37.0 °C throughout the experiment. High-resolution optical microscope images (0.5 μm/pixel) were captured by tiling the entire bottom of each microbatch every 10 min for a minimum of 2 days. This setup enabled reliable detection of micron-sized particles and allowed tracking of solution conditions from clear to nucleation and crystal growth stages. The induction time represents the period between achieving constant supersaturation and the first detection of crystals. Due to the inherent stochasticity of nucleation, induction times measured under identical conditions follow a probability distribution. By conducting a large number of induction time measurements, the cumulative probability distribution function $P(t)$ is determined. This function is then fitted to an analytical expression describing nucleation kinetics (eq 1), allowing for the extraction of key parameters such as the nucleation rate (J) and growth time (t_g).[23] In this expression, V represents the constant system volume.

$$P(t) = 1 - \exp(-JV(t - t_g)) \qquad (1)$$

2.5. Image Processing and Segmentation

Images from the microscope were preprocessed, segmented, and labeled to distinguish individual crystal objects from noncrystal objects. All operations were done off-line, i.e., postexperimentation, using the Image Processing Toolbox in Matlab version 2024a.[24] Preprocessing and segmentation involved the following steps applied sequentially on the raw image files: gray-scaling to flatten the color channels, binarization using a dark foreground polarity and adaptive thresholding based on local pixel intensity statistics, inversion of the polarity of the binarized image, segmented object filling with convex hulling, and refinement of object edges by Canny edge detection on the original gray-scaled image. Preprocessing was tuned in several locally- and globally sensitive parameters to increase signal-to-noise ratios from each set of experimental images individually, i.e., to improve the number and resolution of segmented objects in the preprocessed image sets. Parameter tuning was done using well-established heuristics.[25]

Following image segmentation, the `regionprops` function in Matlab was used to collect the following properties for each segmented object: centroid, bounding box, major axis length, minor axis length, orientation, enclosed area, and eccentricity. All lengths and areas were computed in units of pixels, which were later converted to units of microns using original scale labels burned into the raw images. Centers of detected objects were then tracked using an in-house algorithm so as to allow unique mappings between temporally ordered image sets and segmented object properties in each image. Segmented objects were labeled as crystals if the evolution of the collected properties for the objects satisfied select property thresholds. Specifically, we tuned thresholds for object minimum area, maximum area, and eccentricity to best achieve this nominal classification of crystals from noncrystals. Finally, for crystal objects, characteristic length measures were computed using the geometric mean of the radii of the corresponding ellipse approximation to the object, i.e., $L_c = \sqrt{r_1 r_2}$ where L_c is the characteristic particle length, and r_1 and r_2 represent the major and minor semiaxis radii of the approximating ellipse. All measures were reported in microns. The characteristic lengths of individual crystals of both hydrates in Figure S2 were calculated from segmented time-lapse images within the same experiment (4.0 mM Mg, 0.5 mM PPi, 40 mM Tris buffer, 37 °C, 72 h with 1 h increments). The data represent a single representative crystal of each type, illustrating the relative growth rates of the 6-hydrate and 3.5-hydrate forms.

2.6. Solid-State Characterizations

For Powder X-ray Diffraction (PXRD) analysis shown in Figure 3b, samples were obtained from scaled-up (1 L) crystallizations performed at 0.4 mM and 0.7 mM sodium pyrophosphate concentrations, corresponding to conditions that yield the 6-hydrate and 3.5-hydrate phases, respectively, ensuring sufficient material for reliable phase identification. PXRD data were obtained using a PANalytical X'Pert PRO (∼10 mg sample). For IVT + DNA samples, material collected from the bottom of 96-well plates used for nucleation studies was analyzed using a Bruker D8 VENTURE capillary setup, requiring less than 1 mg of sample. Data were acquired over a 2θ range of 5°−45° using Cu Kα radiation (λ = 1.5406 Å). The resulting diffractograms were compared with simulated PXRD patterns available for Mg_2PPi solid forms. Simulated PXRD patterns, crystal face visualization, and BFDH morphology prediction were performed using Mercury.[26] The BFDH method provides a simple geometrical approach to identify the most relevant crystallographic faces of a given structure based on lattice parameters. Although it does not account for solvent effects, kinetic factors, or nucleation dynamics, it is a widely used tool for guiding experimental face assignments and interpreting observed crystal morphologies.

Scanning Electron Microscopy (SEM) and Energy Dispersive Spectroscopy (EDS) analysis were performed using a Zeiss Gemini 450. Samples were mounted on aluminum stubs with conductive carbon tape and sputter-coated with a thin layer of gold using a Pelco SC-7 Sputter Coater to enhance conductivity. We observed that the particles were fragile, and their edges became damaged during handling and removal from the wells. To mitigate this, crystals were dried within the wells by pipetting out most of the liquid, followed by air-drying the remaining liquid. The bottom of the glass plate was then carefully cut using an engraving pen with a carbide tip, and the detached glass was placed on carbon tape attached to the stub. SEM images were acquired using the SE2 detector to capture surface morphology features. EDS spectra were collected to analyze the elemental composition of the samples, with data processed using AZtec software.

Electron diffraction data were collected using a Thermo Fisher Themis Z STEM microscope operating at 200 kV. The particles were suspended in water and sonicated to break the nanoflowers into smaller fragments, allowing for the study of a single nanopetal. A droplet of this suspension was then deposited onto a TEM grid and dried in a vacuum oven for 2 days. Electron diffraction data were obtained using selected area electron diffraction (SAED) to analyze the crystalline structure and determine the zone axis using CrystBox software.[27] Due to the

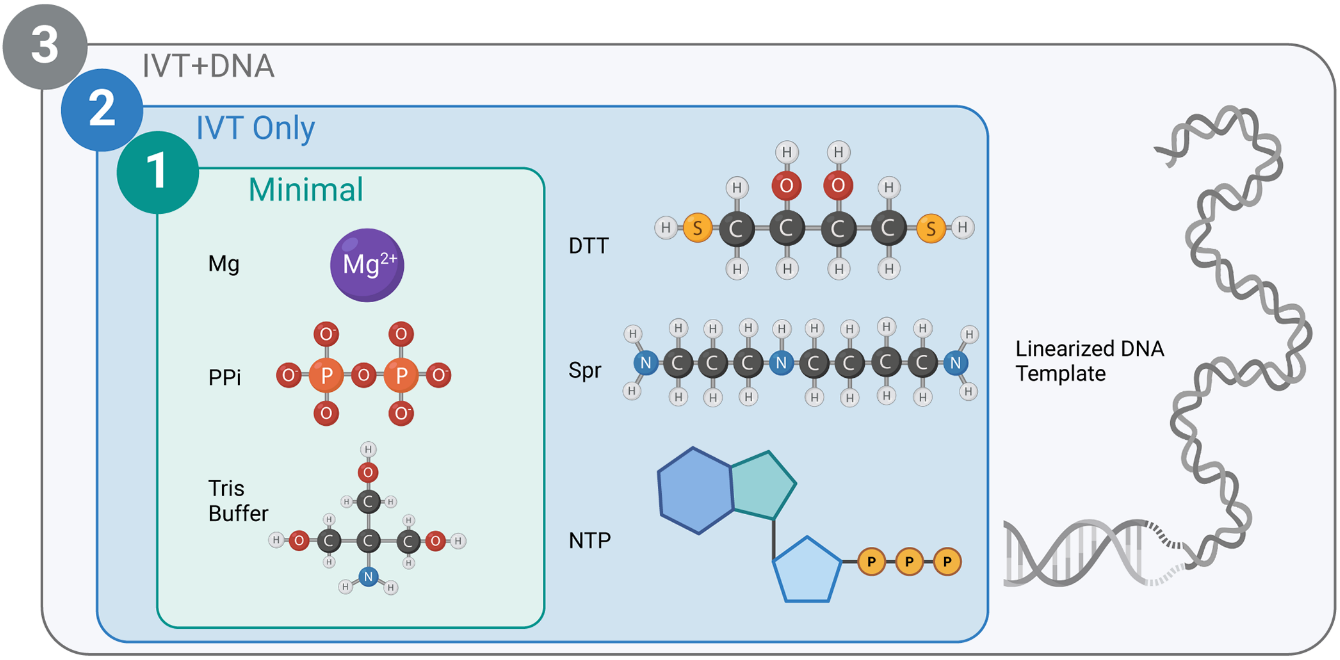

Figure 2. IVT reaction mixture including magnesium (Mg), pyrophosphate (PPi), tris buffer, dithiothreitol (DTT), spermidine (Spr), and nucleotide triphosphate (NTP), and linearized DNA template. The standard IVT mixture was modified by eliminating the T7 RNAP.

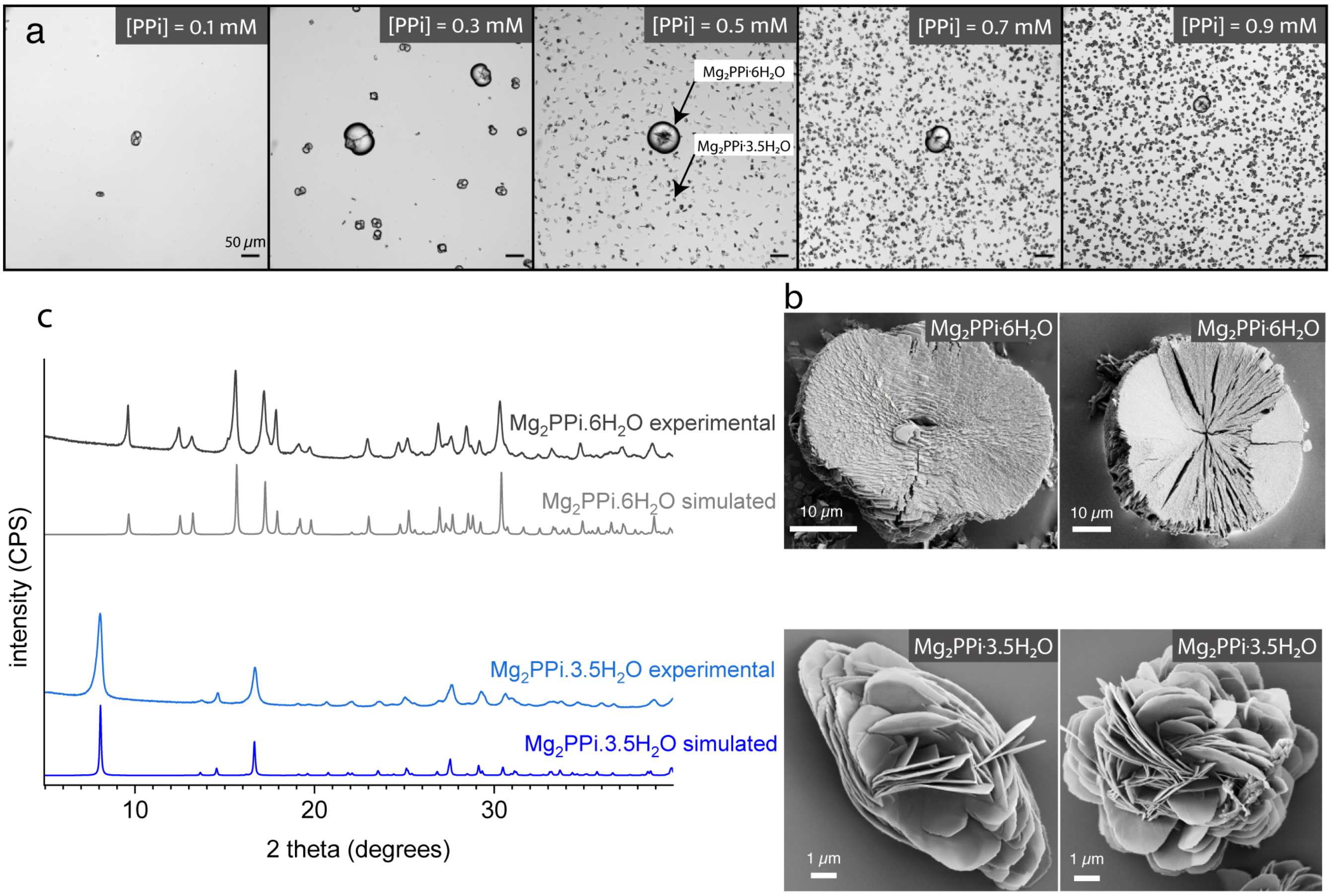

Figure 3. (a) Optical microscope images showing Mg_2PPi crystallization across different PPi concentrations in 40 mM tris buffer with 4 mM $MgCl_2$ after 2 weeks of equilibration. All panels have identical scale bars (50 μm). (b) SEM images highlighting the distinct crystal habits of $Mg_2PPi·6H_2O$ and $Mg_2PPi·3.5H_2O$. (c) Experimental PXRD diffractograms of $Mg_2PPi·3.5H_2O$ and $Mg_2PPi·6H_2O$, overlaid with their respective simulated patterns.

https://doi.org/10.1021/acs.cgd.5c01710

sensitivity of the crystals to the electron beam, prolonged exposure led to their disintegration. To slow down the decomposition process, cryogenic conditions were applied during the data collection to preserve the integrity of the samples for a longer period while collecting electron diffraction data.

2.7. Solubility Measurement

Inductively Coupled Plasma Mass Spectrometry (ICP-MS) was used to measure solubility of the inorganic components using an Agilent 7900 instrument. An 8-point serial dilution of the VeriSpec Magnesium Standard for ICP-MS (10 ppm in 2% HNO_3, Ricca Chemical) was prepared to generate an external calibration curve. Powder samples of $Mg_2PPi{\cdot}3.5H_2O$ and $Mg_2PPi{\cdot}6H_2O$ were dissolved in ultrapure water (VWR Chemicals, with a maximum Mg background of 10 ppt). After one month of equilibration, solutions were filtered, diluted with 2% ICP-grade nitric acid, and analyzed by ICP-MS (MassHunter 5.2).

To develop the phase diagram for $Mg_2PPi{\cdot}3.5H_2O$ in the presence of IVT additives, two 96-well plates were used. One plate contained 4 mM ATP (low ATP), while the other contained 20 mM ATP (high ATP). Various amounts of Mg and PPi were added to each well to populate a 2D grid of conditions, and the plates were left to equilibrate at 37 °C in an incubator. After one month, the well plates were imaged using a Zeiss Axio Observer 7 inverted microscope. Based on the images, the presence or absence of crystals was identified, and this data was used to generate a 2-D grid for thermodynamic modeling (see Figure 4).

To dissolve the nanoflowers and measure the sequestered DNA concentration, EDTA was added. EDTA, which rapidly dissolves DNFs by chelating Mg ions,[13] triggered the dissolution of dried crystals, releasing the trapped DNA. In this experiment, a portion of the clear supernatant above the settled crystals was collected and filtered to check for DNA. The remaining supernatant was removed, and residual ions were washed out by gently adding and removing 200 μL of water three times. Finally, 200 μL of 5 mM EDTA was added to dissolve the crystals, and the resulting solution was analyzed for DNA concentration. A 2 μL sample, diluted by a factor of 2, was analyzed using Capillary Gel Electrophoresis (CGE) on the Agilent FEMTO Pulse system at the MIT BioMicro Center. As a complementary technique, Size Exclusion Chromatography (SEC) was performed using an Agilent BioSec-5 column on a Thermo Vanquish system.

3. RESULTS AND DISCUSSION

3.1. Crystal Structure and Morphology Depend on Solution Conditions

We first investigated the effect of IVT solution conditions on crystal structure by analyzing the solid product of a reactive crystallization of magnesium and pyrophosphate. In the IVT reaction mixture, various ions, small molecules, and macromolecules are present, each of which could influence the crystallization process. To systematically investigate these effects, we divided the experiment into three stages (Figure 2), incrementally introducing components to isolate their impact on crystallization.

In a minimal setup containing only magnesium and pyrophosphate (with Tris buffer to regulate pH), we fixed the Mg concentration at 4 mM and varied PPi from 0 to 1 mM in 0.1 mM increments. The resulting Mg_2PPi crystals (Figure 3a) exhibited two distinct size distributions, both characterized by rounded morphologies and lacking the well-defined edges typically seen in crystalline materials. At low PPi concentrations, a few large crystals were predominant, whereas higher concentrations produced numerous smaller crystals. High-resolution scanning electron microscopy (SEM) (Figure 3b) further revealed that these rounded particles arise from the organization of thin crystalline layers into nanoflower structures. Such formations are commonly referred to as rosette crystal habits in crystallography, where crystals grow in a radial arrangement resembling flower petals.[28]

Powder X-ray Diffraction (PXRD) was then utilized to determine whether the two observed morphologies corresponded to different Mg_2PPi crystal structures. Mg_2PPi has eight polymorphs and hydrates[29−34] and their expected PXRD patterns are shown in Figure S1. The diffractograms (Figure 3c) showed that the two distinct size distributions indeed correspond to two different hydrate forms of Mg_2PPi. The smaller crystals were identified as $Mg_2PPi{\cdot}3.5H_2O$, previously observed in nucleic acid-inorganic hybrid material studies,[9,13] while the larger crystals were characterized as $Mg_2PPi{\cdot}6H_2O$, a hydrate form not previously reported in the context of IVT studies. Given the observed difference in crystal size, we hypothesized that this discrepancy could be linked to the crystal growth rates. To test this, we performed image analysis of time-lapse crystal growth data (Figure S2), which revealed that $Mg_2PPi{\cdot}6H_2O$ crystals grow approximately 8 times faster than $Mg_2PPi{\cdot}3.5H_2O$ crystals, with radial growth rates of 2.25×10^{-10} m/s and 2.76×10^{-11} m/s, respectively, indicating that the size discrepancy arises from growth rate differences between the two hydrate forms. To determine the relative stability of the crystal forms, isolated crystals were equilibrated in fresh solutions, and solubility was measured using inductively coupled plasma mass spectrometry (ICP-MS). The results (Figure S3) indicate that $Mg_2PPi{\cdot}6H_2O$ has significantly lower solubility than $Mg_2PPi{\cdot}3.5H_2O$, suggesting that the commonly observed[13,14] $Mg_2PPi{\cdot}3.5H_2O$ in transcription reactions is the metastable form.

Next, in the "IVT only" setup, we assessed the influence of small molecules present in the IVT reaction on the crystallization behavior of Mg_2PPi by adding Spr, DTT, and ATP to the solution (Figure S4a). The results revealed two key differences compared to the screening without small-molecule additives. First, at low PPi concentrations (0.1 mM), no crystals were observed, suggesting an increase in solubility. Second, the large $Mg_2PPi{\cdot}6H_2O$ crystals disappeared, with only $Mg_2PPi{\cdot}3.5H_2O$ crystals forming across all PPi concentrations.

Finally, in the "IVT + DNA" setup, linearized DNA was added to the mixture to examine its effect on Mg_2PPi crystallization. Specifically, a linearized DNA sequence coding for a self-amplifying RNA (saRNA) construct was added to the solution. This sequence was 11,693 base pairs long and is representative of the longest sequences used in IVT. The DNA concentration was set to 0.59 nM (4.3 ng/μL), within the commonly used range for linearized DNA templates in IVT reactions. At this low concentration, no significant change in the solubility of $Mg_2PPi{\cdot}3.5H_2O$ was expected, and the trend in crystallization yield (Figure S4 a,b) supports this. Additionally, PXRD analysis (Figure S5) confirmed that the crystal form of $Mg_2PPi{\cdot}3.5H_2O$ remained unchanged with and without DNA.

To help understand the solubility trends of our experimental system, we developed a thermodynamic model to predict Mg_2PPi solubility as a function of solution conditions. In our modeling, the thermodynamic supersaturation σ of Mg_2PPi is

$$\sigma = \ln\left(\frac{[Mg^{2+}]^2[PPi^{4-}]}{K_{sp,Mg_2PPi}}\right) \tag{2}$$

where K_{sp,Mg_2PPi} is the solubility product of Mg_2PPi. The exact values of the free ion concentrations $[Mg^{2+}]$ and $[PPi^{4-}]$ are heavily dependent on ionic speciation and were determined by considering the equilibrium concentrations of complexes

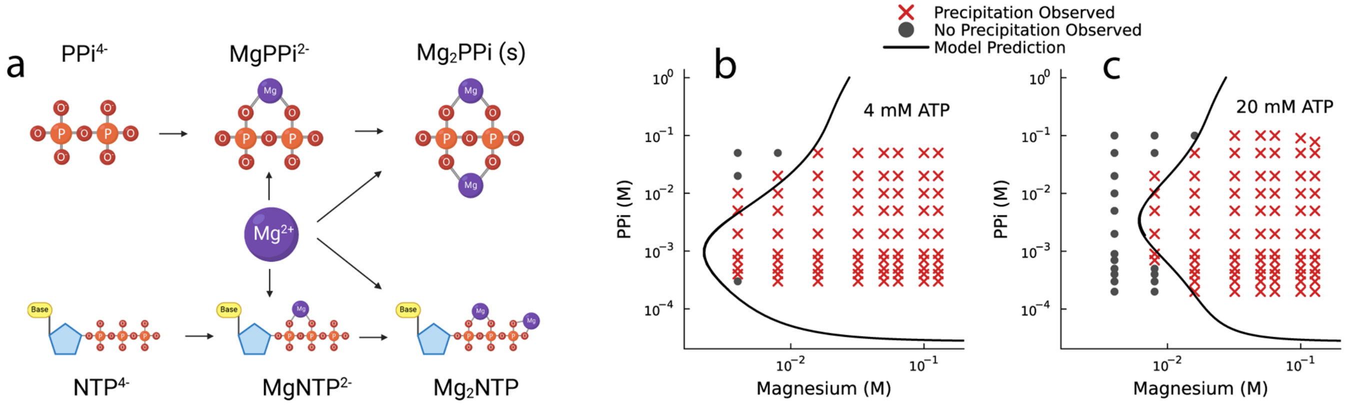

Figure 4. (a) Simplified schematic diagram of speciation network governing magnesium pyrophosphate solubility. Pyrophosphate (PPi) and NTPs compete to bind magnesium. The addition of NTPs is expected to push equilibrium away from Mg_2PPi solid formation. (b,c) Phase diagram comparing experimental precipitation observations with thermodynamic model. Model predictions are shown after fitting of a single solubility constant parameter.

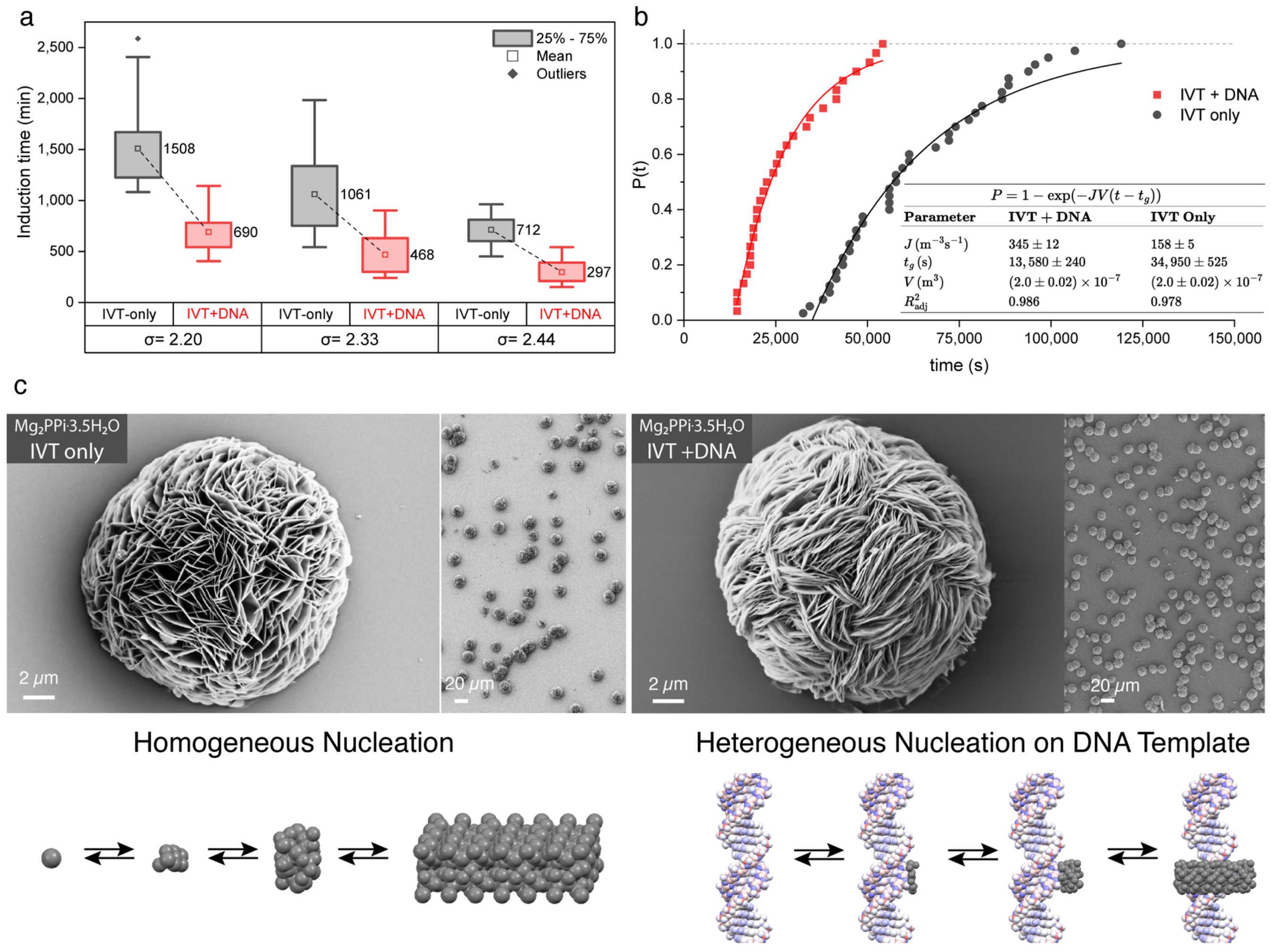

$P = 1 - \exp(-JV(t - t_g))$

Parameter	IVT + DNA	IVT Only
$J\,(\mathrm{m^{-3}s^{-1}})$	345 ± 12	158 ± 5
$t_g\,(\mathrm{s})$	$13,580 \pm 240$	$34,950 \pm 525$
$V\,(\mathrm{m^3})$	$(2.0 \pm 0.02) \times 10^{-7}$	$(2.0 \pm 0.02) \times 10^{-7}$
R^2_{adj}	0.986	0.978

Figure 5. (a) Induction time distribution of Mg_2PPi solid formation at three supersaturation levels, with and without DNA. (b) Cumulative probability distribution of Mg_2PPi crystals at $\sigma = 2.33$, fitted to a Poisson distribution for nucleation rate estimation. (c) SEM images showing the distinct crystal habits of $Mg_2PPi{\cdot}3.5H_2O$ in the presence and absence of DNA in the IVT reaction mixture.

present in the IVT system (Figure 4a).[16] The exact complexes considered and the equilibrium constants used to represent complexation are shown in Supporting Information. This thermodynamic model required fitting a single parameter, K_{sp,Mg_2PPi}, to the solubility measurement of $Mg_2PPi{\cdot}3.5H_2O$ crystals in Tris buffer at 37 °C. After fitting of K_{sp,Mg_2PPi}, model predictions were compared to a phase diagram of Mg_2PPi solubility in conditions representative of IVT (Figure 4b). Ionic speciation is necessary to describe several key trends in these data. For instance, one might expect that adding PPi would

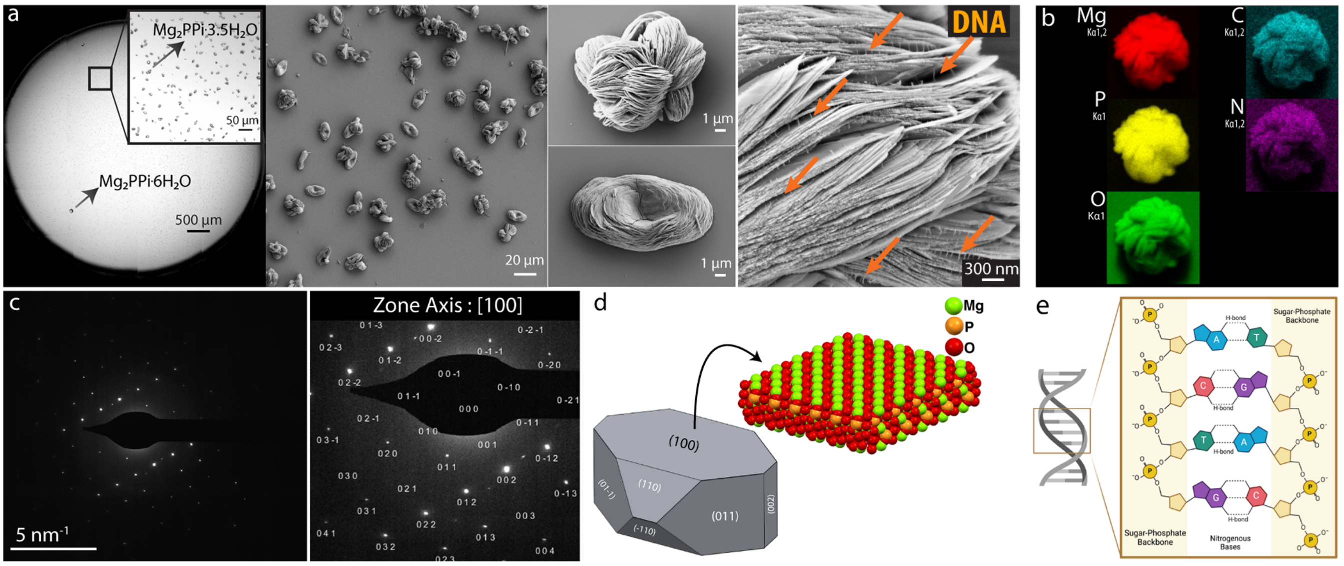

Figure 6. (a) Multiscale images of $Mg_2PPi·3.5H_2O$ with DNA. (b) Elemental mapping (EDS) of the DNF (c) SAED pattern of a single $Mg_2PPi·3.5H_2O$ nanopetal. (d) BFDH morphology prediction for $Mg_2PPi·3.5H_2O$, and packing of ions on {100} face. (e) DNA sugar−phosphate backbone.

decrease the solubility of magnesium due to the formation of insoluble Mg_2PPi. However, counterintuitively, very high (>10 mM) concentrations of PPi can increase the solubility of magnesium in the solution by shifting the equilibrium toward the soluble $MgPPi^{2-}$ species. Moreover, the addition of NTP can increase the solubility of Mg_2PPi since the $MgNTP^{2-}$ and Mg_2NTP complexes serve to sequester free magnesium.

Our modeling approach makes a number of approximations. Primarily, it assumes that the ions in the IVT system are otherwise ideal solutes (i.e., with activity coefficients equal to one). We found that the incorporation of basic activity coefficient models for electrolytic solutions was not necessary for describing trends in data shown. Our results indicate that models which only consider complex formation are suitable for practical use in the range of solution concentrations explored in this work.

3.2. DNA Decreases Induction Time via Template-Induced Crystallization

To better understand the interactions of Mg_2PPi and DNA during nanoflower formation, we measured the kinetics of crystal nuclei formation using optical microscopy. A high-throughput setup was used to accurately estimate the average induction time and nucleation rate.[23,35] Figure 5a shows the induction times for three supersaturation levels with and without DNA, highlighting that the presence of DNA reduces the average induction time by more than half across all supersaturation levels. To extract nucleation rates, the induction times were replotted as cumulative distributions (Figure 5b). Each point corresponds to the time of a single nucleation event, and the width of the cumulative curve reflects the stochastic variation: A broader distribution indicates slower nucleation, whereas DNA produces a steeper curve consistent with faster nucleation. For example, at $\sigma = 2.33$, by fitting the distribution of induction times to a Poisson distribution, we estimated from Figure 5b that the nucleation rate in the presence of DNA increases from 158 ± 5 to 345 ± 12 $m^{-3}\ s^{-1}$. Together, Figure 5a,b demonstrates how DNA shifts the onset of nucleation to earlier times and increases its frequency, as reflected in the steeper cumulative distribution.

The increase in nucleation rate and the significant reduction in induction time in the presence of DNA, despite the low DNA concentration and the lack of changes in solubility, indicates a heterogeneous nucleation mechanism. In other words, DNA does not simply alter bulk solution properties but instead provides a surface that facilitates the local organization of Mg_2PPi precursors, thereby increasing the likelihood of early crystal formation. In the absence of DNA, nucleation is expected to proceed via a homogeneous (spontaneous) pathway. In addition, as seen in the SEM images in Figure 5c, the microstructure of the nanoflowers differs. Most notably, in the absence of DNA the nanopetals are less densely packed, leaving significant internal voids. In contrast, DNA appears to act as a cementing agent, binding the layers together and producing more compact nanoflowers. DNA has been discussed as a templating agent across diverse chemical systems, including facilitating biochemical processes such as primer synthesis in DNA replication,[36] creating functional hybrid systems like tumor-targetable DNA-inorganic nanocomposite aptasensors,[37] and templating the crystallization of calcium phosphate, calcium carbonate, and SiO_2, yielding structures comparable to natural biominerals like tooth enamel and bone.[38]

Finally, we examined the effect of DNA in a system where $Mg_2PPi·6H_2O$ crystals predominated, using a minimal crystallization setup without Spr, DTT, or ATP at low PPi concentration (Figure 3a). In the case of DNA addition, the crystallization product was shifted toward the formation of $Mg_2PPi·3.5H_2O$ crystals (Figure 6). This shift is evident in the PXRD diffractogram, where the $Mg_2PPi·6H_2O$ signal is significantly dampened, and previously undetectable $Mg_2PPi·3.5H_2O$ crystals became predominant (Figure S6). This observation not only supports the templating role of DNA in Mg_2PPi crystallization but also suggests that DNA specifically favors the templating of the $Mg_2PPi·3.5H_2O$ form.

The presence of DNA in DNFs obtained from the minimal setup was confirmed using various methods. High-resolution SEM images (Figure 6a) showed thin vertical lines connecting the nanopetals of Mg_2PPi crystals, which, although not resolving the DNA double helix, indicate DNA's presence due to their absence in the non-DNA case. This indirect evidence supports the idea that these vertical lines represent DNA, as similarly observed in previous work.[9] In these images, DNA strands bind the nanosheets into condensed layers, suggesting that templating occurs at multiple sites along each DNA strand, with additional DNA incorporated during particle growth, consistent with the strong affinity between DNA and Mg_2PPi nanosheets. Energy-dispersive X-ray spectroscopy (EDS) elemental mapping further revealed significant carbon and nitrogen signals in the particles (Figure 6b). Carbon- and nitrogen-rich regions in the DNFs, which have been observed by others,[39] indicate the presence of DNA's organic components within the DNF structure. Finally, analysis of redissolved nanoflower isolate using Capillary Gel Electrophoresis (CGE) and Size Exclusion Chromatography (SEC) showed the presence of DNA (Figure S7). Notably, no DNA was detected remaining in solution after crystallization, indicating that nearly all of the DNA from the initial solution coprecipitated with the $Mg_2PPi \cdot 3.5H_2O$ crystals. This finding explains previous reports on the halting of the IVT reaction upon crystallization, as the essential DNA template is removed from the solution. It also highlights the remarkable DNA capture efficiency of $Mg_2PPi \cdot 3.5H_2O$, suggesting a potential novel approach for recycling DNA after the IVT reaction.

From the depletion of DNA observed by CGE-SEC, we estimate that each nanoflower contains on the order of several million DNA molecules (∼0.1 ng), corresponding to roughly 1% of the total particle mass. Importantly, when the DNA concentration was halved or doubled (down to 0.295 nM and up to 1.18 nM), no changes in induction time or morphology were observed, suggesting that nanoflower formation is robust across this range. A more systematic exploration of DNA concentration effects on nanoflower composition and morphology would be a valuable direction for future studies.

Selected area electron diffraction (SAED) analysis was performed on a single $Mg_2PPi \cdot 3.5H_2O$ nanopetal to investigate the exposed crystalline face (Figure 6c). The [100] crystallographic direction was identified as the zone axis, suggesting that the {100} face plays a key role in the nucleation process by preferentially interacting with DNA's sugar−phosphate backbone (Figure 6e). This also aligns with the largest face predicted by the Bravais-Friedel-Donnay-Harker (BFDH) method (Figure 6d). The precise mechanism of DNA-templated nucleation is likely complex, with sequence- and length-dependent properties of the DNA influencing its templating function. Molecular dynamics simulations indicate that potassium ion populations in DNA's major and minor grooves are highly sequence-specific,[40] and similar effects could occur with Mg ions. Future simulation studies with DNA of varying sequences and lengths could help elucidate the determinants of $Mg_2PPi \cdot 3.5H_2O$ nucleation and orientation.

3.3. Mechanistic Insights into DNA-Templated Crystallization

This work investigates the formation of composite DNA−magnesium pyrophosphate (Mg_2PPi) nanoflowers in the context of *in vitro* transcription. We find that DNA serves as a template for the nucleation of Mg_2PPi crystals during this process and significantly accelerates crystallization. High-throughput kinetics experiments show that the addition of DNA reduces the induction time by more than half. We conclude that this is not due to DNA impacting the supersaturation of Mg_2PPi, as the DNA concentration added is extremely low (<1 nM) and was not found to impact Mg_2PPi solubility. Quantitative estimates indicate that, at these concentrations, DNA can bind less than 0.1% of the total Mg present and represents less than 0.5% of the total nucleotide equivalents in solution, meaning that Mg binding by DNA does not meaningfully alter the free Mg concentration and therefore cannot significantly affect the solubility of Mg_2PPi. Instead, our findings support a template-induced nucleation mechanism,[41] where DNA facilitates the ordered assembly of Mg_2PPi precursors by providing a structural framework. The negatively charged phosphate backbone of DNA likely aligns magnesium ions in solution for nucleation, partially bypassing the stochastic delays associated with homogeneous nucleation. Although DNA remains soluble under the conditions studied, its extended, multivalent architecture enables it to act as a dispersed nucleation scaffold rather than a classical homogeneous additive. In this respect, DNA occupies an intermediate regime between soluble growth modifiers and insoluble polymeric heteronucleants, where spatially fixed coordination motifs are known to convert crystallization inhibitors into nucleation promoters.[42] Similar templating roles of biomolecules are well established in biomineralization, where organic macromolecules guide nucleation and crystal growth into ordered structures[43−45] whereas small molecules or low concentrations of proteins can act as inhibitors[46,47] highlighting that DNA in our system functions analogously to large biomolecules that promote and template mineralization. Notably, this templating effect does not alter the final crystal lattice, as supported by the identical X-ray diffraction patterns of templated and nontemplated $Mg_2PPi \cdot 3.5H_2O$ crystals.

We find that this templating effect is specific to the $Mg_2PPi \cdot 3.5H_2O$ phase. To evaluate the specificity of templating, DNA was added into solution conditions that had been shown to form $Mg_2PPi \cdot 6H_2O$. We found that this addition of DNA redirected crystallization exclusively toward the $Mg_2PPi \cdot 3.5H_2O$ phase, as confirmed by PXRD. The suppression of $Mg_2PPi \cdot 6H_2O$—despite its greater thermodynamic stability and lower measured solubility—further supports the role of DNA in templating the $Mg_2PPi \cdot 3.5H_2O$ phase specifically. Electron diffraction analysis identified the exposed face of the $Mg_2PPi \cdot 3.5H_2O$ nanopetals as the {100} face, suggesting that this face plays a key role in nucleation by preferentially interacting with DNA's sugar−phosphate backbone.

Various characterization techniques confirmed that DNA is sequestered within the nanoflowers. Morphological analysis via electron microscopy, elemental mapping by EDS, and nanoflower redissolution by EDTA (followed by DNA quantification via chromatography and electrophoresis) collectively demonstrate DNA incorporation into the nanoflowers. We find that DNF formation results in a near-complete depletion of DNA from the solution. This finding is consistent with a previous hypothesis that IVT halts upon Mg_2PPi crystallization due to DNA sequestration.[16] This high DNA capture efficiency suggests potential applications for DNA recovery and recycling after IVT, which could improve process efficiency in mRNA production. While our experiments do not include active transcription or continuous pyrophosphate generation, they provide a framework for understanding DNA-mediated templating. Future studies incorporating active IVT could build on this framework to characterize nanoparticles formed during transcription and evaluate implications for DNA recycling and process optimization.

The results of this work offer a new understanding of both the kinetic mechanisms and thermodynamic driving force of DNA

https://doi.org/10.1021/acs.cgd.5c01710

nanoflower formation. Thermodynamic modeling of the speciation network revealed the dependence of Mg_2PPi solubility on solution conditions. As the kinetics of crystallization are linked to this driving force, this modeling approach can be used to predict the dynamics of crystallization in IVT systems. Our results serve as a foundation for future nonenzymatic strategies to mitigate the effects of Mg_2PPi on IVT.

4. CONCLUSION

This study demonstrates that DNA acts as a highly effective template for the nucleation of magnesium pyrophosphate nanoflowers. This templating effect reflects DNA's extended, multivalent architecture, which allows it to act as a dispersed nucleation scaffold, occupying an intermediate regime between soluble growth modifiers and insoluble polymeric heteronucleants. High-throughput kinetics experiments show that DNA reduces the induction time by more than half, supporting a template-induced nucleation mechanism. This templating effect was found to be specific to the $Mg_2PPi{\cdot}3.5H_2O$ phase without any change in the crystal lattice. Various characterization techniques confirmed DNA sequestration within the nanoflowers, resulting in near-complete depletion of DNA from solution. This supports the hypothesis that IVT halts upon Mg_2PPi crystallization due to DNA sequestration and suggests potential for DNA recovery and recycling to improve mRNA production efficiency. By combining kinetic experiments with thermodynamic modeling, we reveal how solution conditions govern crystal formation and provide a predictive framework for controlling crystallization dynamics. These findings lay the foundation for future nonenzymatic strategies to mitigate the effects of Mg_2PPi on IVT.

ASSOCIATED CONTENT

Supporting Information

The Supporting Information is available free of charge at https://pubs.acs.org/doi/10.1021/acs.cgd.5c01710.

Additional experimental data, including X-ray diffraction patterns, growth rate measurements, solubility data of Mg_2PPi hydrates, CGE and SEC analyses of DNA, microscope images, and thermodynamic modeling parameters (PDF)

Time-lapse videos of Mg_2PPi hexahydrate crystallization (MP4)

Time-lapse videos of DNA nanoflower formation in IVT with and without DNA (MP4)

AUTHOR INFORMATION

Corresponding Author

Allan S. Myerson – *Department of Chemical Engineering, Massachusetts Institute of Technology, Cambridge, Massachusetts 02139, United States;* orcid.org/0000-0002-7468-8093; Email: myerson@mit.edu

Authors

Soroush Ahmadi – *Department of Chemical Engineering, Massachusetts Institute of Technology, Cambridge, Massachusetts 02139, United States;* orcid.org/0000-0003-1354-3453

Nathan M. Stover – *Department of Chemical Engineering, Massachusetts Institute of Technology, Cambridge, Massachusetts 02139, United States*

Krystian Ganko – *Department of Chemical Engineering, Massachusetts Institute of Technology, Cambridge, Massachusetts 02139, United States*

Frances B. Kayser – *Department of Chemical Engineering, Massachusetts Institute of Technology, Cambridge, Massachusetts 02139, United States*

Richard D. Braatz – *Department of Chemical Engineering, Massachusetts Institute of Technology, Cambridge, Massachusetts 02139, United States;* orcid.org/0000-0003-4304-3484

Complete contact information is available at: https://pubs.acs.org/10.1021/acs.cgd.5c01710

Notes

The authors declare no competing financial interest.

ACKNOWLEDGMENTS

This research was supported by the U.S. Food and Drug Administration under the FDA BAA-22-00123 program, Award Number 75F40122C00200. Krystian Ganko was further supported by the U.S. Department of Energy, Office of Science, Office of Advanced Scientific Computing Research, Department of Energy Computational Science Graduate Fellowship under Award Number DE-SC0022158. The authors thank the MIT.nano Characterization Facilities for access to SEM and TEM instrumentation. The MIT Center for Environmental Health Sciences (CEHS) is acknowledged for providing access to the ICP-MS instrument.

REFERENCES

(1) Guo, X.; Tian, B.; Li, X.; Lei, Y.; Sun, M.; Miao, Q.; Li, H.; Ma, R.; Liang, H. Aptamer-Loop DNA Nanoflower Recognition and Multicolor Fluorescent Carbon Quantum Dots Labeling System for Multitarget Living Cell Imaging. *ACS Appl. Mater. Interfaces* **2024**, *16*, 45327–45336.

(2) Dai, W.; Zhang, T.; Zhang, F.; Zhang, M. Self-Assembled of Multifunctional Fluorescent Copper-DNA Nanoflowers for Cell-Specific-Target MicroRNA Imaging. *ACS Applied Bio Mater.* **2025**, *8*, 2592–2600.

(3) Roh, Y. H.; Lee, J. B.; Shopsowitz, K. E.; Dreaden, E. C.; Morton, S. W.; Poon, Z.; Hong, J.; Yamin, I.; Bonner, D. K.; Hammond, P. T. Layer-by-Layer Assembled Antisense DNA Microsponge Particles for Efficient Delivery of Cancer Therapeutics. *ACS Nano* **2014**, *8*, 9767–9780.

(4) Zubaite, G.; Simutis, K.; Galinis, R.; Milkus, V.; Kiseliovas, V.; Mazutis, L. Droplet microfluidics approach for single-DNA molecule amplification and condensation into DNA-magnesium-pyrophosphate particles. *Micromachines* **2017**, *8*, 62.

(5) Sun, W.; Ji, W.; Hall, J. M.; Hu, Q.; Wang, C.; Beisel, C. L.; Gu, Z. Self-Assembled DNA Nanoclews for the Efficient Delivery of CRISPR-Cas9 for Genome Editing. *Angew. Chem., Int. Ed.* **2015**, *54*, 12029–12033.

(6) Sun, W.; Jiang, T.; Lu, Y.; Reiff, M.; Mo, R.; Gu, Z. Cocoon-Like Self-Degradable DNA Nanoclew for Anticancer Drug Delivery. *J. Am. Chem. Soc.* **2014**, *136*, 14722–14725.

(7) Zhu, G.; Hu, R.; Zhao, Z.; Chen, Z.; Zhang, X.; Tan, W. Noncanonical Self-Assembly of Multifunctional DNA Nanoflowers for Biomedical Applications. *J. Am. Chem. Soc.* **2013**, *135*, 16438–16445.

(8) Hu, R.; Zhang, X.; Zhao, Z.; Zhu, G.; Chen, T.; Fu, T.; Tan, W. DNA Nanoflowers for Multiplexed Cellular Imaging and Traceable Targeted Drug Delivery. *Angew. Chem., Int. Ed.* **2014**, *53*, 5821–5826.

(9) Kim, E.; Agarwal, S.; Kim, N.; Hage, F. S.; Leonardo, V.; Gelmi, A.; Stevens, M. M. Bioinspired Fabrication of DNA-Inorganic Hybrid Composites Using Synthetic DNA. *ACS Nano* **2019**, *13*, 2888–2900.

(10) Danilevich, V. N.; Mulyukin, A. L.; Machulin, A. V.; Sorokin, V. V.; Kozlov, S. A. Structural variability of DNA-containing Mg-pyrophosphate microparticles: Optimized conditions to produce particles with desired size and morphology. *J. Biomol. Struct. Dyn.* **2019**, *37*, 918−930.

(11) Baker, Y. R.; Chen, J.; Brown, J.; El-Sagheer, A. H.; Wiseman, P.; Johnson, E.; Goddard, P.; Brown, T. Preparation and characterization of manganese, cobalt and zinc DNA nanoflowers with tuneable morphology, DNA content and size. *Nucleic Acids Res.* **2018**, *46*, 7495−7505.

(12) Lee, J. B.; Hong, J.; Bonner, D. K.; Poon, Z.; Hammond, P. T. Self-assembled RNA interference microsponges for efficient siRNA delivery. *Nat. Mater.* **2012**, *11*, 316−322.

(13) Shopsowitz, K. E.; Roh, Y. H.; Deng, Z. J.; Morton, S. W.; Hammond, P. T. RNAi-microsponges form through self-assembly of the organic and inorganic products of transcription. *Small* **2014**, *10*, 1623−1633.

(14) Roh, Y. H.; Deng, J. Z.; Dreaden, E. C.; Park, J. H.; Yun, D. S.; Shopsowitz, K. E.; Hammond, P. T. A Multi-RNAi Microsponge Platform for Simultaneous Controlled Delivery of Multiple Small Interfering RNAs. *Angew. Chem., Int. Ed.* **2016**, *55*, 3347−3351.

(15) Akama, S.; Yamamura, M.; Kigawa, T. A multiphysics model of in vitro transcription coupling enzymatic reaction and precipitation formation. *Biophys. J.* **2012**, *102*, 221−230.

(16) Stover, N. M.; Ganko, K.; Braatz, R. D. Mechanistic modeling of in vitro transcription incorporating effects of magnesium pyrophosphate crystallization. *Biotechnol. Bioeng.* **2024**, *121*, 2636−2647.

(17) Tersteeg, S.; Mrozowich, T.; Henrickson, A.; Demeler, B.; Patel, T. R. Purification and characterization of inorganic pyrophosphatase for in vitro RNA transcription. *Biochem. Cell Biol.* **2022**, *100*, 425−436.

(18) Stover, N. M.; Ahmadi, S.; Rosenfeld, J.; Destro, F.; Myerson, A. S.; Braatz, R. D. Model-Based Optimization of Fed-Batch In Vitro Transcription. *ChemBiochem* **2025**, *26* (21), No. e202500485.

(19) Kwon, H.; Kim, M.; Seo, Y.; Moon, Y. S.; Lee, H. J.; Lee, K.; Lee, H. Emergence of synthetic mRNA: In vitro synthesis of mRNA and its applications in regenerative medicine. *Biomaterials* **2018**, *156*, 172−193.

(20) Zhang, J.; Liu, Y.; Li, C.; Xiao, Q.; Zhang, D.; Chen, Y.; Rosenecker, J.; Ding, X.; Guan, S. Recent Advances and Innovations in the Preparation and Purification of In Vitro-Transcribed-mRNA-Based Molecules. *Pharmaceutics* **2023**, *15*, 2182.

(21) Barbier, A. J.; Jiang, A. Y.; Zhang, P.; Wooster, R.; Anderson, D. G. The clinical progress of mRNA vaccines and immunotherapies. *Nat. Biotechnol.* **2022**, *40*, 840−854.

(22) Erdemir, D.; Lee, A. Y.; Myerson, A. S. Nucleation of Crystals from Solution: Classical and Two-Step Models. *Acc. Chem. Res.* **2009**, *42*, 621−629.

(23) Jiang, S.; Ter Horst, J. H. Crystal Nucleation Rates from Probability Distributions of Induction Times. *Cryst. Growth Des.* **2011**, *11*, 256−261.

(24) *The MathWorks Inc., MATLAB version: 24.1(R 2024a)*. MathWorks, Inc.2024

(25) Gonzalez, R.; Woods, R. *Digital Image Processing, Global ed.*, 4th ed.; Pearson International: New York, NY, USA, 2017.

(26) Macrae, C. F.; Sovago, I.; Cottrell, S. J.; Galek, P. T. A.; McCabe, P.; Pidcock, E.; Platings, M.; Shields, G. P.; Stevens, J. S.; Towler, M.; Wood, P. A. Mercury 4.0: From visualization to analysis, design and prediction. *J. Appl. Crystallogr.* **2020**, *53*, 226−235.

(27) Klinger, M. More features, more tools, more CrysTBox. *J. Appl. Crystallogr.* **2017**, *50*, 1226−1234.

(28) Schneer, C. J. *Mineralogy*; Springer US: Boston, MA, 1983; pp. 98−103.

(29) Calvo, C. The Crystal Structure of alpha-Mg2P2O7. *Acta Crystallogr.* **1967**, *23*, 289.

(30) Calvo, C. Refinement of the Crystal Structure of beta-Mg2P2O7. *Can. J. Chem.* **1965**, *43*, 1139−1146.

(31) Zhai, S.; Gu, X.; He, Y.; Xue, W.; Yang, H. Phase Transition of α-Mg2P2O7 at High-Pressure and High-Temperature Conditions: The Third Polymorph of Mg2P2O7. *Inorg. Chem.* **2024**, *63*, 19701−19706.

(32) Kongshaug, K. O.; Fjellvåg, H.; Lillerud, K. P. Synthesis and crystal structure of the hydrated magnesium diphosphate Mg2P2O7 · 3.5H2O and its high temperature variant Mg2P2O7 · H2O. *Solid State Sci.* **2000**, *2*, 205−214.

(33) Souhassou, M.; Lecomte, C.; Blessing, R. H. Crystal Chemistry of Mg2P2O7.nH2O, n = 0, 2 and 6: Magnesium-Oxygen Coordination and Pyrophosphate Ligation and Conformation. *Acta Crystallogr.* **1992**, *48* (4), 370−376.

(34) Ahmadi, S.; Müller, P.; Myerson, A. S. Magnesium Pyrophosphate Octahydrate (Mg2P2O7 · 8H2O): Structure and Properties. *Inorg. Chem.* **2025**, *64*, 18968−18974.

(35) Goh, L.; Chen, K.; Bhamidi, V.; He, G.; Kee, N. C. S.; Kenis, P. J. A.; Zukoski, C. F. I. I. I.; Braatz, R. D. A Stochastic Model for Nucleation Kinetics Determination in Droplet-Based Microfluidic Systems. *Cryst. Growth Des.* **2010**, *10*, 2515−2521.

(36) He, Q.; Lin, X.; Chavez, B. L.; Agrawal, S.; Lusk, B. L.; Lim, C. J. Structures of the human CST-Polα-primase complex bound to telomere templates. *Nature* **2022**, *608*, 826−832.

(37) Kim, N.; Kim, E.; Kim, H.; Thomas, M. R.; Najer, A.; Stevens, M. M. Tumor-Targeting Cholesterol-Decorated DNA Nanoflowers for Intracellular Ratiometric Aptasensing. *Adv. Mater.* **2021**, *33* (11), 2007738.

(38) Athanasiadou, D.; Carneiro, K. M. M. DNA nanostructures as templates for biomineralization. *Nat. Rev. Chem.* **2021**, *5*, 93−108.

(39) Kim, E.; Zwi-Dantsis, L.; Reznikov, N.; Hansel, C. S.; Agarwal, S.; Stevens, M. M. One-Pot Synthesis of Multiple Protein-Encapsulated DNA Flowers and Their Application in Intracellular Protein Delivery. *Adv. Mater.* **2017**, *29* (26), 1701086.

(40) Pasi, M.; Maddocks, J. H.; Lavery, R. Analyzing ion distributions around DNA: Sequence-dependence of potassium ion distributions from microsecond molecular dynamics. *Nucleic Acids Res.* **2015**, *43*, 2412−2423.

(41) Parambil, J. V.; Poornachary, S. K.; Heng, J. Y. Y.; Tan, R. B. H. Template-induced nucleation for controlling crystal polymorphism: From molecular mechanisms to applications in pharmaceutical processing. *CrystEngcomm* **2019**, *21*, 4122−4135.

(42) Pfund, L. Y.; Price, C. P.; Frick, J. J.; Matzger, A. J. Controlling Pharmaceutical Crystallization with Designed Polymeric Heteronuclei. *J. Am. Chem. Soc.* **2015**, *137*, 871−875.

(43) Du, C.; Falini, G.; Fermani, S.; Abbott, C.; Moradian-Oldak, J. Supramolecular Assembly of Amelogenin Nanospheres into Birefringent Microribbons. *Science* **2005**, *307*, 1450−1454.

(44) Qin, K.; Zheng, Z.; Wang, J.; Pan, H.; Tang, R. Biomineralization strategy: From material manufacturing to biological regulation. *Giant* **2024**, *19*, 100317.

(45) Katase, F.; Kajiyama, S.; Kato, T. Macromolecular templates for biomineralization-inspired crystallization of oriented layered zinc hydroxides. *Polym. J.* **2017**, *49*, 735−739.

(46) Hunter, G. K.; Hauschka, P. V.; Poole, R. A.; Rosenberg, L. C.; Goldberg, H. A. Nucleation and inhibition of hydroxyapatite formation by mineralized tissue proteins. *Biochem. J.* **1996**, *317*, 59−64.

(47) Duchstein, P.; Schodder, P. I.; Leupold, S.; Dao, T. Q. N.; Kababya, S.; Cicconi, M. R.; de Ligny, D.; Pipich, V.; Eike, D.; Schmidt, A.; et al. Small-Molecular-Weight Additives Modulate Calcification by Interacting with Prenucleation Clusters on the Molecular Level. *Angew. Chem., Int. Ed.* **2022**, *61* (40), No. e202208475.